Received: 9 July 2024 | Revised: 7 November 2024 | Accepted: 30 December 2024

DOI: 10.1002/aic.18733

AIChE JOURNAL

RESEARCH ARTICLE

Process Systems Engineering

Magnetic particle capture in high-gradient magnetic separation: A theoretical and experimental study

Marko Tesanovic[1] | J. Pedro de Souza[2] | Martin Z. Bazant[2,3] | Sonja Berensmeier[1,4]

[1]Technical University of Munich, School of Engineering and Design, Chair of Bioseparation Engineering, Garching, Germany

[2]Department of Chemical Engineering, Massachusetts Institute of Technology, Cambridge, Massachusetts, USA

[3]Department of Mathematics, Massachusetts Institute of Technology, Cambridge, Massachusetts, USA

[4]Technical University of Munich, Munich Institute of Integrated Materials Energy and Process Engineering (MEP), Garching, Germany

Correspondence
Marko Tesanovic, Technical University of Munich, School of Engineering and Design, Chair of Bioseparation Engineering, Boltzmannstraße 15, 85748 Garching, Germany.
Email: m.tesanovic@tum.de

Funding information
Federel Ministry of Food and Agriculture, Grant/Award Number: BMLE 281A503A19

Abstract

High-gradient magnetic separation (HGMS) has traditionally been used in mineral processing, with many effective models developed for typically employed rod-wire shaped matrices. However, its potential in bioprocessing, especially for high-value products, introduces new demands on plant and matrix design. This study presents a multi-scale model for HGMS that simulates new complex geometries, which enhance particle recovery. We have developed microscopic models to accurately simulate the trajectories of magnetic particles within the fluid flow and magnetic fields of HGMS systems. A pivotal aspect of our work is the effective translation of microscopic relationships into macroscopic transport models. The model is validated experimentally using a rotor-stator HGMS system tailored for bioprocessing, with magnetic particle concentration measurements showing strong alignment with the model's predictions. The model's flexibility enables its application across various matrix shapes, overcoming the limitations of traditional rod-wire models, and providing a robust framework for improved HGMS in-silico process understanding and optimization.

KEYWORDS
downstream processing, magnetic particle, magnetic separation, multi-scale modeling

1 | INTRODUCTION

High-gradient magnetic separation (HGMS) has evolved considerably since its early 20th-century applications, particularly in mineral processing and wastewater treatment. Devices like the Frantz (1937) and Jones Separators (1976) set the foundation,[1] with Kolm's[2] introduction of fine ferromagnetic filament matrices in the 1970s marking a key advancement. These developments helped establish HGMS as a powerful method for separating weakly magnetic materials from complex mixtures.

Recently, HGMS has found utility in innovative bio-separation processes and biomedical applications.[3] In the realm of biotechnology, HGMS technology offers a unique combination of efficiency, selectivity, and gentle processing conditions for isolating and purifying biomolecules, cells, and other biological targets from complex mixtures in high-throughput.[4] This process involves using magnetic particles or beads, which are typically coated or functionalized to ensure selectivity, to label biological entities of interest. Recent studies demonstrate HGMS's effectiveness in bioprocessing, such as lactoferrin separation from whey,[5] and rAAV5 purification achieving significant impurity reduction.[6] This innovative approach holds significant implications for bio-manufacturing,[7] therapeutics, and diagnostics.[4] However, bioprocessing introduces new demands on plant and matrix design, especially for high-value products. A pivotal aspect of HGMS in

bioprocessing is the need for gentle processing, enhanced particle recovery, resuspension, and mixing of magnetic particles, while also ensuring effective clean-in-place (CIP) systems to maintain matrix hygiene.[8] These unique requirements call for more complex geometries beyond the traditional fine filaments and rod-wire shaped matrices.

HGMS operates on a principle similar to deep filtration, as illustrated in Figure 1. The process involves a filter chamber filled with a ferromagnetic material, known as the matrix, which is traditionally designed with wire-shaped rods and placed within an external magnetic field. However, the matrix can take any geometry to effectively concentrate the magnetic field, creating zones that attract magnetic particles. These particles adhere to the matrix, allowing the purified fluid to exit the system. Once the matrix is saturated, the magnetic field is deactivated, the particles are flushed out, and the cycle is repeated.

Theoretical approaches have been integral to HGMS development from the beginning, with mechanistic models forming the foundation of understanding particle capture characteristics through magnetic fields and fluid dynamics. While these models have been rigorously studied and refined, they are limited in scope, primarily addressing the needs of mineral processing and wastewater treatment, where rod-wire matrices are primarily used. Our study advances HGMS modeling beyond traditional rod-wire matrix designs, focusing on advanced bio-processing specific designs and applications.

The theory of HGMS merges the physics of magnetic fields with fluid hydrodynamics. Analytical solutions for the magnetic fields around traditional rod-wire and spherical matrices have been established since Straton's work in 1941 on infinitely long rods, forming a foundation for magnetic separation studies.[9] Similarly, modeling concentration and loading profiles in HGMS has become straightforward once kinetic relationships and mass balances are established.[1] Several studies have primarily focused on the capture characteristics of wire-based matrices. These include Watson's early works, which introduced key concepts such as capture radius,[10] a metric pivotal in determining whether a particle will be captured by the wire matrix. This capture radius is derived through numerical solutions to the equation of magnetic particle motion within a high-gradient magnetic field. Further, Watson developed the dependency of particle trajectories on the velocity ratio of magnetic and flow fields.[11] In 1982, Gerber et al.[12] extended Watson's model by considering the decline in capture efficiency caused by particle buildup. This is important because particle accumulation on the wire matrix alters the surrounding flow and magnetic fields, reducing the overall capture efficiency. Investigations have also extended to various configurations of wire matrices, including unstructured steel-wool matrices,[11] screw thread rods,[13] and longitudinal vs. transversal matrix configurations,[14] with numerical and experimental studies consistently focusing on rod-wire matrices or small variations,[15] like elliptic shapes.[16] More recently, another study utilized a coupled finite element method (FEM) and finite volume method (FVM) approach to simulate the magnetic field and fluid field, respectively.[17] In this study, magnetic field gradients obtained from FEM were incorporated into the nodes of finite volumes for force computation, facilitating the calculation of the capture radius as formulated by Watson.[17] The second part of the study investigated particle buildup shapes using the discrete element method (DEM) for particle simulation. Addressing inaccuracies arising from the simplifications in previous studies, Choomphon-anomakhun et al. proposed a more advanced model.[18] Their approach involves modeling the magnetic field using Laplace's equation. Independently,

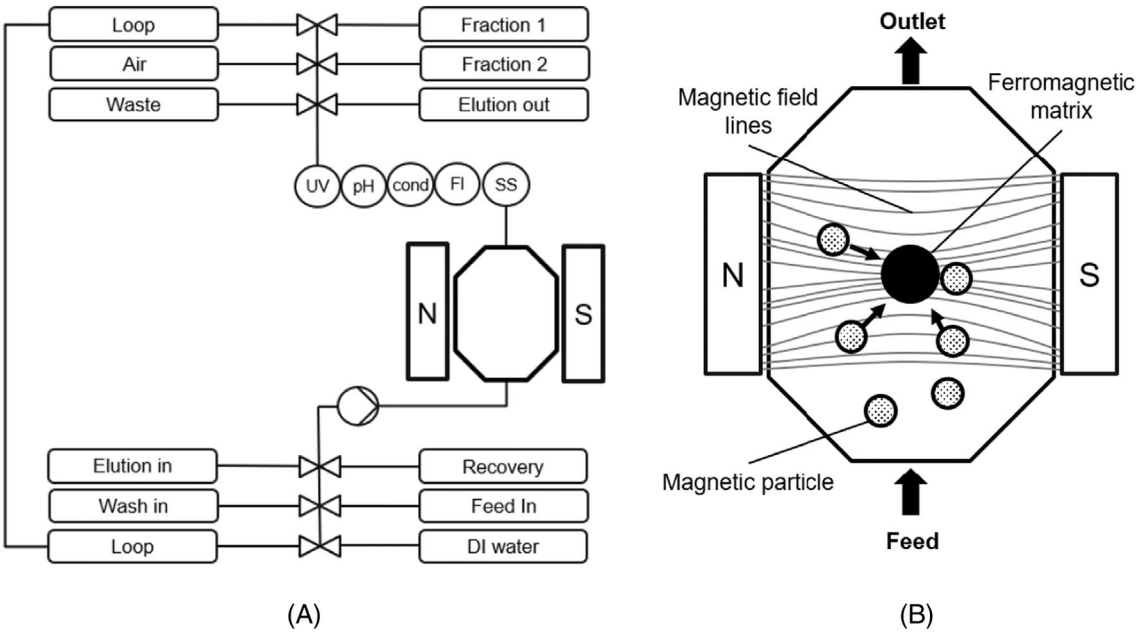

FIGURE 1 (A) Simplified piping and instrumentation diagram (PID) for an HGMS plant, illustrating the valve blocks, the magnetically surrounded chamber, sensor configuration, and the recirculation loop. (B) Diagram of the HGMS chamber and matrix, illustrating the principle of magnetic particle capture in high-gradient magnetic fields.

the flow field and particle transport are modeled using the compressible Navier–Stokes equation. Magnetic force, fluid force, and the force due to diffusion are introduced as external forces in the particle transport equation, including the screening effect of particle buildup on the magnetic field.[18]

Despite the significant progress in HGMS theory, these traditional approaches have been largely developed for rod-wire matrices used in mineral processing and wastewater treatment and do not readily translate to more complex geometries required for bioprocessing applications. In bioprocessing, where gentle processing, recovery, and resuspension of magnetic particles are essential, more intricate matrix designs beyond rod-wire geometries are needed. Currently, there is no straightforward methodology available to model HGMS with arbitrary matrix designs. The process for converting microscopic model data of a wire into a macroscopic balance equation through a probability function is well-established by Watson.[10] However, applying this approach to matrix designs beyond rod-wire shapes introduces complexities. To address this, we extended the second probability equations by Watson[10] to accurately represent more complex matrix geometries, like disc-shaped matrices with holes. Furthermore, there is a notable absence of approaches to simulate the complete HGMS process for bio-molecule purification on a macroscopic level. In response to this gap, we propose a multi-scale model approach. This involves extracting theoretical insights from a microscopic modeling scale and integrating them into macroscopic mass balances to simulate the entire HGMS process used in biomolecule purification. While our experimental focus is on the RS-HGMS design, our proposed model approach is versatile, allowing for the simulation of any matrix design. Furthermore, our study aims to incorporate the effect of entrapped fluid within the captured magnetic particles. This trapped fluid, retained by the magnetic particles, accumulates into a deposit of considerable volume, which substantially affects the process's dynamics and efficiency. However, the scope of our investigation will primarily concentrate on the behavior of magnetic particles within the HGMS process.

2 | THEORY

The model of HGMS comprises several transport and sorption processes on different scales. Molecules in solution are transported through the interstitial bulk volume between the HGMS matrix by convective flow. In the chamber, the molecules are also subject to dispersion due to eddies and other flow inhomogeneities. The separation mechanism, rooted in ferrohydrodynamics, enables the efficient separation of magnetic particles or magnetically labeled molecules from complex mixtures. Table 1 at the end of this chapter lists all the key parameters used in the modeling for this study.

2.1 | Macroscopic models

In our research, we consider an RS-HGMS chamber, as depicted in a simplified schematic in Figure 2C. This chamber is characterized by its height h, radius R and includes a ferromagnetic matrix of multiple discs with a designated volume V_{matrix}. Into this chamber, a mixture comprising various molecular species, labeled as $i = 1,\ldots,N_c$, is introduced at the inlet of the column with the velocity $\boldsymbol{u}_0$. It is assumed that each of these components is homogeneously distributed across the cross-sectional areas of the chamber's interstitial volume.

In our study, we consider two distinct phases: (1) the mobile phase, which is the fluid region, shown as the white area in Figure 2C, and (2) the stationary phase, representing the volume occupied by the ferromagnetic matrix, which is depicted by the bounding surfaces B_5 and B_6 in 2B. The matrix is modeled as a homogenized structure, which is particularly justified by the uniform spacing of numerous magnetic discs throughout the separator, as shown in 2C. The transport of molecules through the interstitial spaces of the ferromagnetic matrix occurs via convective flow, constituting the mobile phase. Within the chamber, dispersion arises from eddies and flow irregularities. Magnetic particles or magnetically labeled molecules are captured on the matrix surface, functioning as the stationary phase. It should be noted that while the solid stationary phase is not porous, the captured magnetic particles form a separate stationary slurry phase, representing the mass of retained particles on the matrix. The concentration in this case refers to the amount of particles per chamber volume, not the solid material itself. Given the radial symmetry of the matrix in our RS-HGMS system, all molecules are assumed homogeneously distributed over cross-sections, and the concentrations in the mobile and stationary slurry phase, denoted as $c_i^l(t,z)$ and $\sigma_i^s(t,z)$ respectively, are only functions of the axial position z. Here, σ_i^s

TABLE 1 Key physical parameters used in this work.

Denotation	Unit	Value
$D_{ax,st}$: Axial dispersion coefficient for static discs	$\frac{m^2}{s}$	0.5×10^{-6}
$D_{ax,dyn,80}$: Axial dispersion coefficient for rotating discs at 80% speed	$\frac{m^2}{s}$	0.4×10^{-4}
D_{demag}: Demagnetization factor[21]	—	0.5 (cylinder), 0.33 (sphere)
h: Height of chamber	m	0.2
$\boldsymbol{H}_0$: External applied magnetic field strength	$\frac{A}{m}$	2.227×10^5
$\boldsymbol{M}_{sat,p}$: Magnetization saturation of BIONs	$\frac{A}{m}$	3.5×10^5
$\boldsymbol{M}_{sat,m}$: Magnetization saturation of matrix[26]	$\frac{A}{m}$	1.3×10^6
n: Number of matrix discs	—	25
R: Radius of chamber	m	0.1
γ: Rate constant for deposition rate	—	2
ϵ_0: Porosity of empty chamber	—	0.91
μ_0: Vacuum magnetic permeability	$\frac{N}{A^2}$	1.257×10^{-6}
μ_f: Fluid magnetic permeability	$\frac{N}{A^2}$	μ_0
μ_m: Initial matrix magnetic permeability[27]	$\frac{N}{A^2}$	$\mu_0 \times 10^3$
$\chi_{p,0}$: BION magnetic susceptibility at zero field	—	5.83

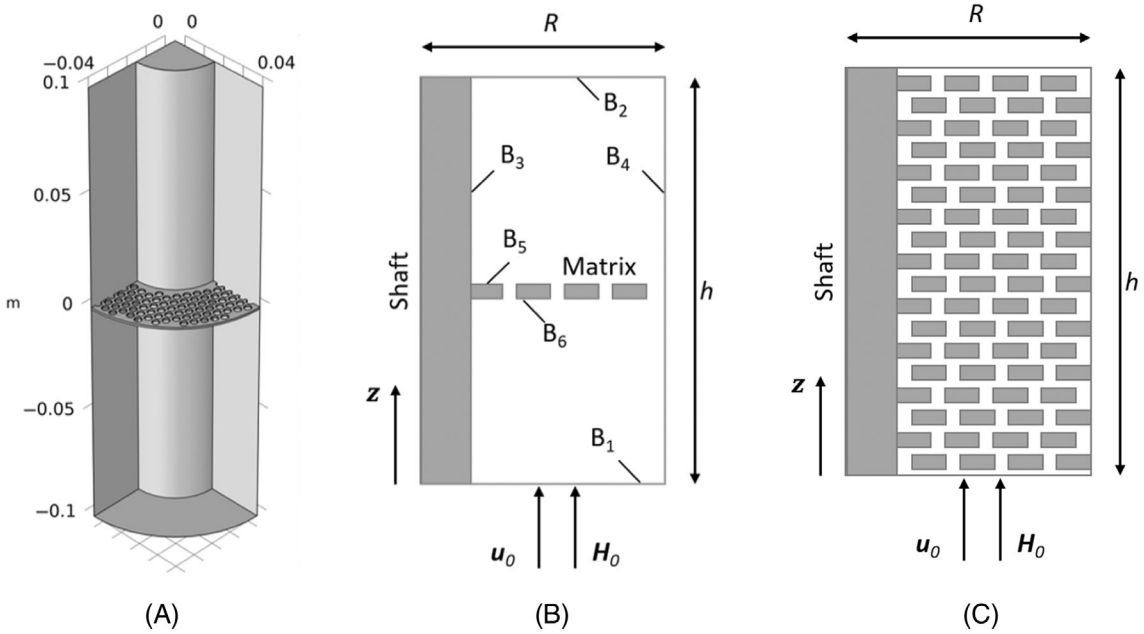

FIGURE 2 (A) Three-dimensional domain of a quarter of the RS-HGMS chamber with a single ferromagnetic matrix disc. Magnetic particles are captured on the matrix with perforated holes, positioned at the center of the annulus channel with height *h* and radius *R*. (B) Schematic of a two-dimensional cut area in the *z* axis of (A). A uniform external magnetic field $\boldsymbol{H}_0$ and average inlet flow velocity $\boldsymbol{u}_0$ are applied in the direction perpendicular to the matrix at the bottom. B_1 toB_6 are indicating boundaries. (C) Schematic of a two-dimensional cut area in the *z* axis with multiple discs.

represents the mass of particles retained per unit volume of the chamber, V_c, and c_i^l corresponds to the mass of particles in suspension per unit volume of the interstitial volume, V_{int}. We are homogenizing the uptake of particles on the multiple matrix discs, effectively assuming a porous medium model for the conservation equations and flow dynamics. This approach assumes uniform behavior across the separator's matrix discs, streamlining the computational complexity of our simulations. It is crucial to recognize that retained magnetic particles encapsulate fluid among themselves, forming a slurry volume, V_{slurry}, described by the following volume fraction:

$$\frac{V_{slurry}(t,z)}{V_c} = \alpha \frac{\sigma_i^s(t,z)}{\rho_i}, \tag{1}$$

where α denotes the ratio of the total slurry volume to the particle volume in the retained slurry and ρ_i is the density of molecule *i*. The porosity of the chamber unit, denoted as $\epsilon(t,z)$, is given by the relation:

$$\epsilon(t,z) = \epsilon_0 - \alpha \frac{\sigma_i^s(t,z)}{\rho_i}, \tag{2}$$

with ϵ_0 being the initial porosity of the empty chamber containing the matrix. Previous studies have often neglected the impact of the retained fluid, based on the assumption that the term $\alpha \frac{\sigma_i^s(t,z)}{\rho_i}$ is significantly smaller than ϵ_0. However, our experimental findings, particularly with bare iron oxide nanoparticles (BIONs), challenge this assumption. In fact, our experiments indicate that the factor α is approximately 25 in pure water, as detailed in the results chapter.

The general mass balances in the system incorporate the accumulation rate along with transport by convection and axial dispersion, which can be described by Equation (3). To maintain simplicity, the sigma term σ_i^s is solely accounting for magnetic particles in the system, intentionally excluding non-magnetic components:

$$\frac{\partial}{\partial t}[c_i^l \epsilon + \sigma_i^s] = -u_0 \frac{\partial c_i^l}{\partial z} + D_{ax} \frac{\partial^2 c_i^l}{\partial z^2} \tag{3}$$

Here, u_0 denotes the inlet flow velocity, and D_{ax} represents the axial dispersion coefficient. It is important to note that the uptake of the particles onto the stationary phase has been homogenized over z, so that the σ_i^s term is considered as a volumetric uptake term over the whole chamber length, thus averaging over each ferromagnetic matrix along the column. We modeled the recirculation system using a flow sheet approach that distinguishes between two sections: the chamber and the external piping/valve section. The external piping and valve sections are treated as ideal plug flow systems, where only convective transport is considered. The volumes of the external piping and valve components have been accounted for in the overall system volume for the mass balance.

While the mass balance equation is formulated independently of the specific magnetic capture mechanism, determining the rate of capture of magnetic particles $\frac{\partial \sigma_i^s}{\partial t}$, necessitates an understanding of the underlying microscopic processes. It is essential to integrate the

functions of the elementary ferrohydrodynamic processes into these macroscopic mass balances.

Drawing inspiration from the works of Herzig et al.,[19] Watson defined two separation probabilities to bridge the microscopic understanding with the macroscopic models, particularly in the context of a rod wire matrix[10,11]:

1. Retention probability $p_1 = \frac{\text{Number of retained particles}}{\text{Number of entering particles}}$,
2. Capture radius probability $p_2 = \frac{\text{Effective capture area}}{\text{Total cross-sectional area}}$.

In this study, we modified the expression for the probability p_2 to accommodate more complex matrix geometries beyond the traditional wire-shaped matrices. Consider a small time interval Δt, during which the number of retained particles increases by $\frac{\partial \sigma_i^s}{\partial t}\Delta t \Delta z$. The number of particles entering the element in this interval is $c_i^l u_0 \Delta t$. Consequently, the probability p_1, representing the likelihood of a particle being captured, can be expressed as[10]:

$$p_1 = \frac{\frac{\partial \sigma_i^s}{\partial t}\Delta z}{c_i^l u_0}, \tag{4}$$

Watson introduced the concept of an effective capture radius for a rod-wire matrix, where any particle entering this radius is captured by the matrix. However, more complex geometries, like those in the RS-HGMS matrix, require a more generalized approach. We extended Watson's second probability by introducing an effective capture area, A_{eff}, defined by a factor a_{eff}, ranging from 0% to 100% of the total cross-sectional area A_c. The effective capture area per unit length of the chamber is expressed as $A_{\text{eff}} = a_{\text{eff}} A_c \frac{n}{h} \Delta z$, where n represents the number of plates in the chamber. This formulation assumes a uniform matrix distribution across the chamber. The probability p_2 is then calculated accordingly:

$$p_2 = \frac{A_c n \Delta z a_{\text{eff}}}{A_c h}, \tag{5}$$

This methodology, employing a generalized effective capture area, is adaptable to any matrix geometry. It is crucial to underscore that the boundary conditions tailored for a specific geometry must be correspondingly adjusted in the microscopic models, as detailed in the methodology section.

Utilizing Equations (4) and (5), the kinetic equation describing the capture rate of magnetic particles is given by:

$$\frac{\partial \sigma_i^s}{\partial t} = \frac{n a_{\text{eff}} c_i^l u_0}{h} G, \tag{6}$$

where the function G is incorporated to account for the deposition rate onto the matrix surface. Gerber et al. proposed the following expression for G[12]:

$$G = 1 - \left(\frac{\sigma_i^s}{\sigma_{i,\max}^s}\right)^{\gamma}, \tag{7}$$

with $\sigma_{i,\max}^s$ representing the maximum number of particles that can be captured per unit volume of the chamber. Equation (7) can also be seen as the probability of deposition. Assuming Langmuir adsorption where each particle forms a monolayer, thereby excluding one particle volume, the parameter γ equals 1, which represents the probability of finding a vacancy. However, due to the disordered nature of deposits and potential multi-layer growth, the excluded volume effect diminishes, facilitating a higher deposition rate. This behavior is empirically reflected by setting gamma to 2 in this model. It has been observed that for $\gamma \approx 2$, a poly-disperse fraction of magnetic particles aligns well with experimental results.[11] For very high values of gamma, the model predicts that nearly all particles are captured until they reach the limiting density.

In scenarios involving a rod-wire matrix, the effective capture radius or area can be analytically determined by solving a boundary value problem using cylinder functions that satisfy Laplace's equation. However, for matrices with more complex geometries, this analytical method becomes less feasible. Therefore, we propose a numerical approach that is applicable to any matrix geometry.

2.2 | Microscopic models

To accurately model the RS-HGMS system, it is essential to understand the influence of the magnetic field on particle trajectories. Our microscopic models, based on Newton's second law, account for magnetic and fluid drag forces. Using the specific geometry from Figure 2A, we calculate the effective capture area a_{eff}, which is then integrated into the macroscopic models.

2.2.1 | Magnetic field

In the context of static fields and under the assumption of the absence of magnetic monopoles, the magnetic scalar potential ϕ^{M} is governed by Laplace's equation. This potential can be expressed for both the matrix and the liquid domains, denoted as $\phi_{\text{m}}^{\text{M}}$ and $\phi_{\text{l}}^{\text{M}}$ respectively, as follows:

$$\nabla^2 \phi_{\text{m}}^{\text{M}} = 0, \tag{8a}$$

$$\nabla^2 \phi_{\text{l}}^{\text{M}} = 0. \tag{8b}$$

The magnetic field strength $\mathbf{H}$ in each region is derived from the scalar potential by the gradient, as given by the equation

$$-\nabla \phi^{\text{M}} = \mathbf{H}. \tag{9}$$

The magnetic flux densities in the matrix and the liquid are then defined by

$$\boldsymbol{B}_{\text{m}} = \mu_0 (\boldsymbol{M}_{\text{m}} + \boldsymbol{H}_0 - \nabla \phi_{\text{m}}^{\text{M}}), \tag{10}$$

$$\boldsymbol{B}_{\mathrm{l}} = \mu_0(\mathbf{M}_{\mathrm{l}} + \boldsymbol{H}_0 - \nabla\phi_{\mathrm{l}}^{\mathrm{M}}). \tag{11}$$

The externally applied uniform magnetic field strength in the z direction is denoted as $\boldsymbol{H}_0$, and μ_0 represents the magnetic permeability of vacuum. The magnetization in the matrix and liquid phases, $\boldsymbol{M}_{\mathrm{m}}$ and $\boldsymbol{M}_{\mathrm{l}}$ respectively, correspond to the induced magnetization, which is related to the external magnetic field $\boldsymbol{H}_0$. For the liquid phase, we assume a magnetization close to zero in diluted magnetic particle suspensions (less than 1% volume fraction). It is established that $\boldsymbol{M}_i = \Delta\chi\boldsymbol{H}_{\mathrm{in}}$ is the induced magnetic field intensity for a material or component i, with $\boldsymbol{H}_{\mathrm{in}} = \boldsymbol{H}_0 - \boldsymbol{H}_{\mathrm{demag}}$.[20] Here, $\Delta\chi$ is the susceptibility difference between material i and the carrier fluid. In the case where the magnetic susceptibility of the particles χ_i is significantly larger than that of the carrier fluid χ_l, the fluid susceptibility can be neglected, leading to $\Delta\chi = \chi_i$. The magnetic poles induced inside a body tend to overlay the background magnetic field, usually directing the field lines opposite to those of the external field. This effect is quantified by introducing the demagnetization factor D_{demag}. With self-demagnetization defined as $\boldsymbol{H}_{\mathrm{demag}} = \boldsymbol{M}_i D_{\mathrm{demag}}$, the matrix magnetization can be determined from its inherent material properties[20]:

$$\boldsymbol{M}_{\boldsymbol{m}} = \begin{cases} \dfrac{\chi_{\mathrm{m},0}}{1 + D_{\mathrm{demag}}\chi_{\mathrm{m},0}}\boldsymbol{H}_0 & \text{if} \quad \dfrac{\chi_{\mathrm{m},0}}{1 + D_{\mathrm{demag}}\chi_{\mathrm{m},0}}\boldsymbol{H}_0 < \boldsymbol{M}_{\mathrm{sat,m}}, \\ \dfrac{M_{\mathrm{sat,m}}}{H_0}\boldsymbol{H}_0 & \text{if} \quad \dfrac{\chi_{\mathrm{m},0}}{1 + D_{\mathrm{demag}}\chi_{\mathrm{m},0}}\boldsymbol{H}_0 \geq \boldsymbol{M}_{\mathrm{sat,m}}, \end{cases} \tag{12}$$

where $\chi_{\mathrm{m},0}$ denotes the magnetic susceptibility of the ferromagnetic matrix in the absence of an external magnetic field, while $\boldsymbol{M}_{\mathrm{sat,m}}$ represents the saturation magnetization of the ferromagnetic matrix. The demagnetization factor is typically 1 for a flat oblate spheroid when the external field is perpendicular to the flat side and 0.5 when the field is aligned with the flat side.[21] In our system, the presence of densely covered holes in the disc matrix alters the geometry, resembling a configuration closer to cylindrical shapes. For this reason, we approximate the demagnetization factor to 0.5, corresponding to cylindrical shapes.[21]

2.2.2 | Flow field

We model the fluid as inviscid, simplifying the Navier–Stokes equations to the Euler equation by excluding viscosity. The validity of this approximation depends on the Reynolds number, with higher values generally justifying the assumption of inviscid flow as inertial effects dominate over viscous effects, though this limit is also associated with turbulent conditions. In our system, Reynolds numbers range between 5 and 40, depending on the flow rate and including the constrictions and wider regions in the chamber, indicating a transition from laminar to potentially turbulent flow. This range, however, suggests a regime where viscous effects could still be significant, making the inviscid assumption a first simple approximation of our fluid flow. Additionally, at the scale of individual particles, we assume a low Reynolds number to justify the use of Stokes drag. Assuming the fluid is irrotational on the scale of the HGMS chamber, the velocity $\mathbf{u}$ is described by a potential function ϕ^F:

$$-\nabla\phi^F = \boldsymbol{u}. \tag{13}$$

Considering the fluid's velocity field to be divergence-free, the potential ϕ^F adheres to Poisson's equation:

$$-\nabla^2\phi^F = 0. \tag{14}$$

Regarding the boundary conditions, the inlet is controlled by a Neumann condition on boundary B_1 (Figure 2B), where the initial velocity $\boldsymbol{u}_0$ is set. The outlet B_2 acts as a free outflow and the potential ϕ^F is set to zero with a Dirichlet condition.

2.2.3 | Particle dynamics

The trajectories of individual particles under the influence of combined flow and magnetic fields are determined by balancing the hydrodynamic drag force with the magnetic force. Particle motion is modeled using the Lagrangian approach, based on Newton's second law:

$$m_i\frac{\partial\boldsymbol{u}_i}{\partial t} = \sum\boldsymbol{F}_{\mathrm{extern}}, \tag{15}$$

where $\mathbf{F}_{\mathrm{extern}}$ represents the sum of external forces acting on component i, with m_i and $\mathbf{u}_i$ denoting its mass and velocity, respectively. These forces include Brownian motion, hydrodynamic, gravitational, and inter-particle forces.[22] For particles smaller than 10 μm in diluted suspensions, gravitational, buoyancy,[23] and inertia forces[19] can be neglected. Brownian motion may have a notable effect, but it is generally overshadowed by magnetic and Stokes' drag forces.[23] It's essential to distinguish between scales, as viscosity becomes critical at the particle level, introducing complexity with drag forces, unlike the inviscid assumption at the chamber scale. Such distinctions are crucial for a coherent understanding of the flow dynamics and the forces acting on the particles. The Stokes' drag force is defined by:[11]

$$\boldsymbol{F}_{\mathrm{d},i} = 6\pi\eta r(\boldsymbol{u} - \boldsymbol{u}_i), \tag{16}$$

where η, r, $\boldsymbol{u}$, and $\boldsymbol{u}_i$ are the fluid viscosity, particle radius, fluid velocity, and particle velocity, respectively.

The magnetic force is modeled using an effective dipole moment approach, where the magnetized particle is represented by an "equivalent" point dipole.[24] The force exerted on this dipole, and thus on the particle, is expressed as:

$$\boldsymbol{F}_{\mathrm{m},i} = \mu_f(\boldsymbol{m}_{i,\mathrm{eff}} \cdot \nabla)\boldsymbol{H}, \tag{17}$$

where μ_f and $\boldsymbol{m}_{i,\mathrm{eff}}$ are the fluid permeability and the effective dipole moment of the particle, respectively. The effective dipole moment for

a magnetizable particle is $\boldsymbol{m}_{i,\text{eff}} = V_i \boldsymbol{M}_i$, with V_i being the particle volume.[20] The magnetization $\boldsymbol{M}_i$ is defined as per Equation (12), but for a spherical particle, the demagnetization factor is $\frac{1}{3}$.[22] Consequently, the magnetic force on particle i can be expressed as[25]:

$$\boldsymbol{F}_{\text{m},i} = \mu_f V_i (\boldsymbol{M}_i \cdot \nabla)\boldsymbol{H}, \tag{18}$$

By balancing the magnetic force in Equation (18) and the hydrodynamic force in Equation (16), and neglecting the inertial effect, the governing equations for particle trajectory can be obtained:

$$\boldsymbol{u}_i = \boldsymbol{u} - \frac{2\mu_f r^2}{9\eta}(\boldsymbol{M}_i \cdot \nabla)\boldsymbol{H}. \tag{19}$$

2.2.4 | Effective capture area

Considering Equation (19), the effective capture area of a multi-layer matrix is influenced by several factors: the characteristic magnetic force, the flow field, the matrix configuration, and the number of matrix layers or repeating units. Assuming that the accumulation of magnetic particles does not affect the magnetic and flow fields, the magnetic field strength is determined solely by the system geometry, the applied local field $\boldsymbol{H}$, and the particle magnetization $\boldsymbol{M}_\text{i}$. The characteristic magnetophoretic velocity $\boldsymbol{u}_{\text{m},i}$ for a single component i is derived from Equation (19) by setting the background fluid velocity $\boldsymbol{u}$ to zero and using the height of the matrix disc as the characteristic length:

$$\boldsymbol{u}_{\text{m},i} = -\frac{2\mu_f r^2}{9\eta h}\boldsymbol{M}_i \boldsymbol{H}. \tag{20}$$

This magnetophoretic velocity encapsulates the effects of the characteristic magnetic force as well as the geometry and configuration of the matrix. The number of repeating units in the matrix is considered in Equation (5). As a result, the dimensionless effective capture area a_{eff} can be represented as a function of $\frac{u_\text{m}}{u_0}$, as suggested by Watson.[11]

3 | MATERIALS AND METHODS

3.1 | Experiments

3.1.1 | RS-HGMS

For experimental validation, we utilized a commercially available rotor–stator high-gradient magnetic separator (RS-HGMS, MES-25 RS, Andritz KMPT GmbH, Germany). A comprehensive description of the system[7] and validation of its cGMP compliance[8] have been previously published for its predecessor, the MES-100 RS. Contrary to the 1.0 L magnetic separation chamber described therein, our system is equipped with a smaller 0.25 L magnetic separation chamber, comprising 13 rotor and 12 stator discs (made of high-grade steel 1.4016, with a profile roughness parameter Ra of 0.4 μm and electropolished). The discs are perforated with holes (diameter = 3 mm, arranged in a grid pattern with 4 mm spacing and a minimum web width of 1 mm). The same RS-HGMS system, including identical piping, instrumental setup, and in-line analytics, is described in.[5] For our system, the external piping and valves, which are outside the magnetic separation chamber, contribute an additional volume of approximately 350 mL, ensuring a complete account of the system's fluid volume.

3.1.2 | Synthesis of BIONs

Bare iron oxide nanoparticles (BIONs) were synthesized using the co-precipitation method, as described by Roth et al.,[28] and following the experimental protocol of Krolitzki et al.[5] While comprehensive characterization data were previously published in,[5] key characteristics relevant to our simulations were specifically analyzed in this study. After synthesis, the BIONs were divided into six batches and subjected to extensive washing with purified water. This process continued until the wash water conductivity was reduced below 200 µS cm^{-1} to ensure the removal of residual synthesis by-products.

3.1.3 | Characterization of BIONs

For offline quantification of BIONs in pure water, we utilized a gravimetric method, drying 1 mL of BIONs suspension in 1.5 mL reaction tubes for at least 24 h inside a drying cabinet. After drying, the mass of the BIONs was determined.

As indicated by Equations (16) and (18), the forces on BIONs in a magnetic and flow field are influenced by their size. Therefore, we measured the hydrodynamic diameter of the BIONs, defined as the diameter of a theoretical sphere exhibiting the same behavior as the respective agglomerate. This measurement was conducted using dynamic light scattering (DLS) in triplicates with 1 mL of 1 g L^{-1} BIONs suspensions at 25°C, using a Zetasizer Ultra (Malvern Pananalytical GmbH, Kassel, Germany). For evaluation, we used the volume distribution to accurately represent the size distribution of the BIONs in the suspension.

For the analysis of magnetic susceptibility, lyophilized BIONs samples were fixed in a small tube. The magnetic field was varied from −4 to +4 T, while maintaining a stable temperature of 300 K, using a superconducting quantum interference device (SQUID, Quantum Design MPMS XL-7).

3.1.4 | Magnetic filter capacity BIONs

In this study, the maximum filtering capacity of the separator chamber, denoted as $\sigma^s_{i,\text{max}}$, was determined through breakthrough studies with BIONs across various size distributions and pump velocities. A BION slurry in water, with a constant concentration, was pumped through the magnetized matrix chamber from the bottom to the top.

Samples were collected at the outlet at 5-s intervals to detect BIONs breakthrough via dry measurements. The maximal filter capacity, $\sigma^s_{i,\max}$, was computed from the breakthrough curves using the integral:

$$\sigma^s_{i,\max} = \int_{t_{\text{start}}}^{t_{\text{end}}} c^{\text{I}}_i \frac{\dot{V}}{V_c}\, dt. \tag{21}$$

3.1.5 | Soft-sensor BIONs concentration

To enable the measurement of BION concentration during a full RS-HGMS run, where discrete sample collection is not feasible, we developed a soft-sensor. This soft-sensor integrates the online density measurement capability of the Coriolis flow meter[5] with a mathematical model. Utilizing the measured total density ρ_{total}, the known density of water ρ_{water} as a function of temperature T, and the density of BIONs ρ_{BION}, the concentration of BIONs in pure water can be calculated using the following equation:

$$c_{\text{BION}} = \frac{\rho_{\text{total}} - \rho_{\text{water}}(T)}{1 - \frac{\rho_{\text{water}}(T)}{\rho_{\text{BION}}}}. \tag{22}$$

The accuracy of the soft-sensor was validated through comparison with breakthrough curves, which were established by collecting samples for dry measurements.

3.1.6 | Entrained fluid volume of BION-Slurry in pure water

To determine the volume of entrained liquid within the captured BIONs, we employed two experimental methods: (1) a displacement experiment and (2) residence time measurement. In the displacement experiment, the system was initially filled with water, then drained using air, and the displaced water volume was recorded. In the second run, the system was filled with BIONs to matrix capacity, and again drained with the magnet active. The difference in displaced water volumes between the two runs provided the volume occupied by the slurry, including magnetic particles and entrained liquid. For the residence time experiments, we calculated the volume difference between an empty and a fully loaded chamber based on residence time measurements. This volume corresponds to the BION slurry.[29] A 1 mol L^{-1} sodium chloride solution served as a tracer, with concentration monitored via an online conductivity sensor.[5]

3.2 | Simulation

The macroscopic models for mass balance simulation have been implemented using MATLAB R2023b. The microscopic models are numerically solved utilizing COMSOL Multi-physics V5.6. The methodologies and specifics of these simulation approaches are detailed in the following two subsections.

3.2.1 | Macroscopic models

Model Equations 1 to 7 form a system of non-linear partial differential algebraic equations (PDAEs). These equations are discretized spatially in z using finite volumes and the first-order upwind scheme, resulting in ordinary differential equations (ODEs). To mitigate numerical dispersion inherent in low-order schemes, a sensitivity analysis was conducted to establish an appropriate grid size, ensuring minimal dispersion effects. After spatial discretization, we solve the resulting initial value problem for the system of ODEs using a fully implicit method, employing the ODE15s solver. For poly-dispersed magnetic particle sizes, we selected ten discrete sizes from the particle-size distribution, based on equal volume divisions of the magnetic particles. Two key parameters were calibrated: the axial dispersion coefficient in the static state of the discs, $D_{\text{ax, st}}$, and the axial dispersion coefficient in the rotating state, $D_{\text{ax,dyn,80}}$, when the discs rotate at 80% intensity. Both were fitted to experimental data to ensure the model's accuracy.

3.2.2 | Mircoscopic models

COMSOL Multi-physics is used to solve the Laplace equation (Equations 8a–14), determining the distributions of magnetic and flow fields in the 3D domain (Figure 2A). We simulate magnetic particle trajectories across this domain using Equation (19) to calculate the effective capture area. In this process, 500,000 uniformly distributed particles are released at boundary B_1 (Figure 2B), and those contacting the matrix are considered trapped. The effective capture area a_{eff} is defined as the ratio of trapped particles to those released. By varying inflow velocity $\boldsymbol{u}_0$, we determine the dimensionless effective capture area a_{eff} as a function of $\frac{u_m}{u_0}$. Boundary conditions are as follows: Zero flux at B_3 and B_4; flux condition $\boldsymbol{B}_0$ at B_1; Dirichlet boundary at B_2, setting magnetic potential $\phi_{\text{I}}^{\text{M}}$ to $\frac{B_0(y-0.5h)}{\mu_f}$. The matrix surface boundaries B_5 and B_6 are set as $-\mathbf{n}\nabla\phi^M = \pm\mathbf{M}_m$. Fluid flow uses a Neumann condition at B_1 and a zero-potential Dirichlet boundary at B_2, with zero flux for other boundaries.

4 | RESULTS AND DISCUSSION

4.1 | BIONs characterization

The SQUID measurements, shown in Figure A2 in the Appendix, display a typical superparamagnetic curve for BIONs, with a saturation magnetization of 67.62 emu, g^{-1} and no noticeable remanence or hysteresis at 0 T. This confirms the superparamagnetic behavior of the BIONs. Additionally, the initial magnetic susceptibility, $\chi_{i,0}$, calculated from the slope at zero field, is 5.83. Both values are crucial input parameters for the model.

We analyzed the hydrodynamic diameters of BIONs across six batches, as shown in Figure A1in the Appendix, with particle sizes ranging from 100 to 8000 nm. Batches 2, 3, and 4 had a higher proportion of smaller particles than Batches 1, 5, and 6. Despite

consistent synthesis conditions, variations in particle-size distributions arose due to environmental factors and media characteristics.[4] Conductivity measurements varied between 100 and 200 μS, cm^{-1}, with pH levels from 7 to 9, affecting the zeta potential and resulting in different agglomeration behaviors. The hydrodynamic diameter serves as a crucial input for our models, and these batch variations provide a broader range for validation. It's important to note that particle size is also influenced by the presence of a magnetic field, with agglomerates becoming larger[4] and aligning with the field direction.[30] Given the complex factors at play, we used dynamic light scattering (DLS) measurements as a representative approximation of particle size. Overall, the characterization of BIONs in our study aligns closely with the findings in,[5] due to the use of the same synthesis protocols and laboratory settings. Additional BION properties that are not directly relevant to our modeling objectives can be found in the referenced work.[5]

4.2 | Characterization of magnetic filter capacity

The maximum loading capacity $\sigma^s_{i,\max}$ of the separation matrix was determined from the breakthrough curves in Figure 5A,B and Equation (21). Table 2 presents the total maximum BION mass captured, which is convertible to $\sigma^s_{i,\max}$ using the chamber volume V_c. Results show variability in maximum mass depending on flow rate and BION size distribution. Higher flow rates reduce maximum loading due to increased fluid velocity and hydrodynamic drag, as seen at 1880 mL min^{-1}, where capacity was 36.4 g. While the capacity was expected to remain stable for constant volume flows, it varied between 41.3 and 50.4 g, likely due to particle size differences.

In Figure 5A graph B4 at an initial concentration of 4.7 g L^{-1} exhibits an early breakthrough of BIONs. Graph B4, corresponding to Batch 4, shows the smallest BIONs distribution size in the range 200–500 nm (Figure A1, Appendix). This early breakthrough within the first 400 s supports the model's prediction that smaller particles experience weaker magnetic forces, resulting in less effective separation.

Ultimately, it is evident, that $\sigma^s_{i,\max}$ is influenced by factors such as BION agglomerate size, volume flow, and the magnetic properties of BIONs, including magnetic susceptibility. Therefore, for each new batch of BIONs and varying volume flows, $\sigma^s_{i,\max}$ requires specific calibration in our experimental setup.

4.3 | Characterization of entrained fluid volume

The entrained volume between captured BIONs on the matrix was evaluated using two methods: (1) residence time measurement and (2) displacement measurement, as detailed in the methodology. Figure A3 shows residence time results for an empty versus fully loaded chamber. The average residence time for the fully loaded chamber was 45.5 ± 2.1 s (triplicate), compared to 71.1 ± 1.4 s (duplicate) for the empty chamber. At a flow rate of 8.3 mL s^{-1}, the difference in free fluid volume was 212.4 mL, correlating to the slurry volume. For 46 g of BIONs, the fluid-to-particle volume ratio α was 23.9. Displacement measurements, also in triplicate, gave a volume of 235.2 ± 4.4 mL for 48 g of BIONs, with an α value of 25.5. Both methods suggest α is around 24–25 in pure water. Given the chamber's free volume of 255 mL, the slurry occupies a substantial portion, significantly affecting total porosity during separation.

4.4 | Validation of models

4.4.1 | Magnetization and flow field around the matrix

Figure 3A presents a contour plot depicting the local magnetic field $\boldsymbol{H}$ around the matrix. Notably, the magnetic field strength exhibits an approximate twofold increase around the perforated holes at the edges, relative to the externally applied field. This observation is consistent with existing literature on various rod and ellipsoid-shaped matrices.[1] Additionally, there is a strong decrease in the magnetic field $\boldsymbol{H}$ within the holes, characterizing the matrix in total as a magnetic sieve. The rectangular shape with numerous perforations promotes a more uniform particle capture along the extensive edges of its multiple openings, thereby enhancing separation efficiency through an increased number of edge sites for particle capture. Figure 3B reveals a significant increase in flow velocity through the holes, with velocities up to four times higher than those in the bulk fluid. Overall, the behavior of both the magnetic field $\boldsymbol{H}$ and flow velocity $\boldsymbol{u}$ is consistent with physical expectations, illustrating logical and coherent patterns in these potential fields.

Utilizing the simulated magnetic field and potential flow field, we analyzed magnetic particle trajectories, represented as streamlines in Figure 4A. These streamlines depict how certain particle paths culminate at the disc, indicating capture, while others traverse through the holes, implying non-capture. Variations in the ratio of magnetic velocity to inflow velocity affect the number of captured particles and consequently, the effective area a_{eff}, as shown in Figure 4B.

Commencing from the origin, the effective area as a function of magnetic and potential flow velocity displays a modified S-shaped curve in Figure 4B. Initially, there is a rapid rise, followed by a gradual saturation towards a value of one. This pattern aligns with the physical principle that an increase in magnetic velocity relative to potential flow

TABLE 2 Maximum filter capacity for the breakthrough curves B1 to B6 in Figure 5.

Curve	B1	B2	B3	B4	B5	B6
$\sigma^s_{i,\max} \times V_c$ (g)	41.3	48.6	36.4	43.6	50.4	47.9
$\dot{V}$ [ml min^{-1}]	650	1120	1880	1487	1400	1430

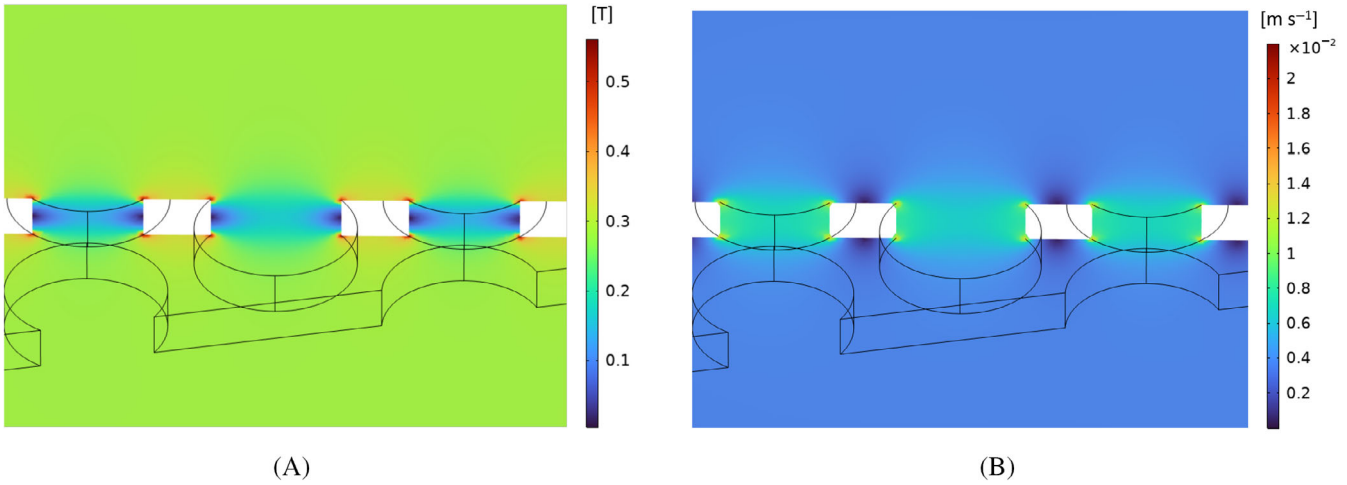

FIGURE 3 Contour plots of (A) magnetic flux density $\boldsymbol{B}_l = \mu_f \boldsymbol{H}_0$ and (B) potential flow field velocity $\boldsymbol{u}$ around a single disc collector. The external applied magnetic field is $\boldsymbol{B}_0 = \mu_0 \boldsymbol{H}_0 = 0.28$ T. The external applied flow field velocity is $\boldsymbol{u} = 5 \times 10^{-3}$ m s^{-1}. Other parameters are provided in Table 1.

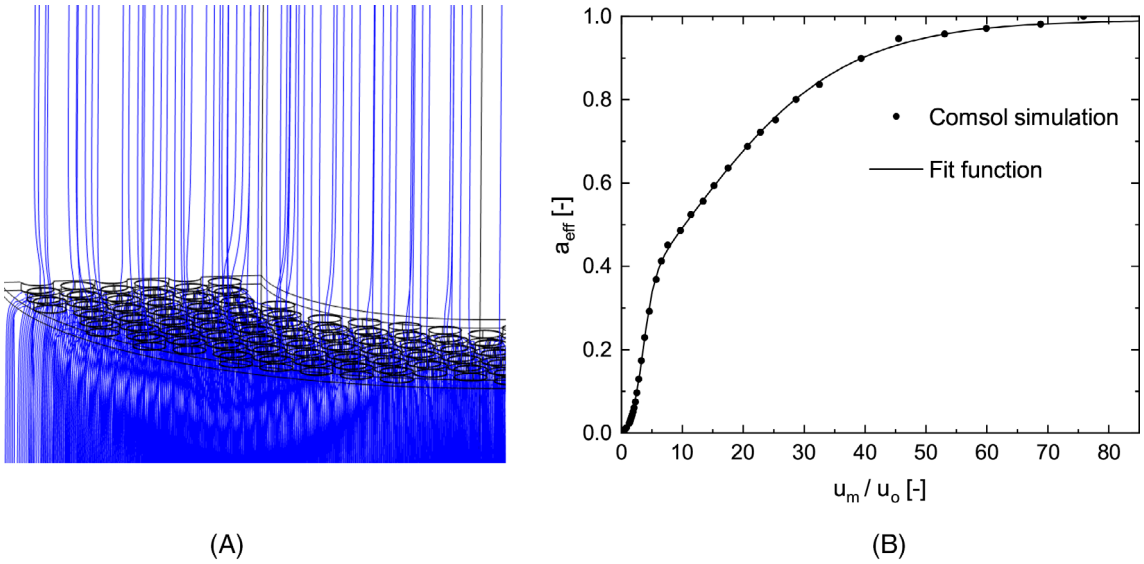

FIGURE 4 (A) Depicts trajectories of 1000 magnetic particles along streamlines ascending from the bottom to the top. By systematically altering the magnetic velocity-to-flow velocity ratio, the points in (B) are obtained. (B) Illustrates the determination of the dimensionless effective capture area. The functional relation is represented using a modified Gompertz function as best fitting curve.

velocity enlarges the effective capture area. Conversely, at zero magnetic velocity, the effective area reduces to zero. To derive a functional relationship for macroscopic models, a modified Gompertz function was employed to describe the relationship between a_{eff} and $\frac{u_m}{u_0}$:

$$a_{\text{eff}} = \frac{1}{1 + a_1 e^{-p\frac{u_m}{u_0}} + a_2 e^{-q\frac{u_m}{u_0}} + a_3} \tag{23}$$

The coefficients for the modified Gompertz function were determined with 95% confidence bounds as follows: $a_1 = 2.035$ (range: 1.8989 to 2.172), $a_2 = 107.1$ (range: 72.27 to 142), $a_3 = -0.00808$ (range: −0.01381 to −0.00234), $p = 0.07477$ (range: 0.07113 to 0.07841) and $q = 1.083$ (range: 0.9909 to 1.175).

With Equation (23) we can complement Equation (6) in order to be able to describe magnetic particles in our RS-HGMS system fully with our macroscopic balances. In the next sub-chapters, we validate our macroscopic models experimentally.

4.4.2 | Breakthrough curves

The model's accuracy was assessed by comparing experimental data with simulation outcomes across varying initial concentrations, velocities, and particle-size distributions. The influence of initial BION concentration on separation efficiency is depicted in Figure 5A. It was observed that an increase in initial

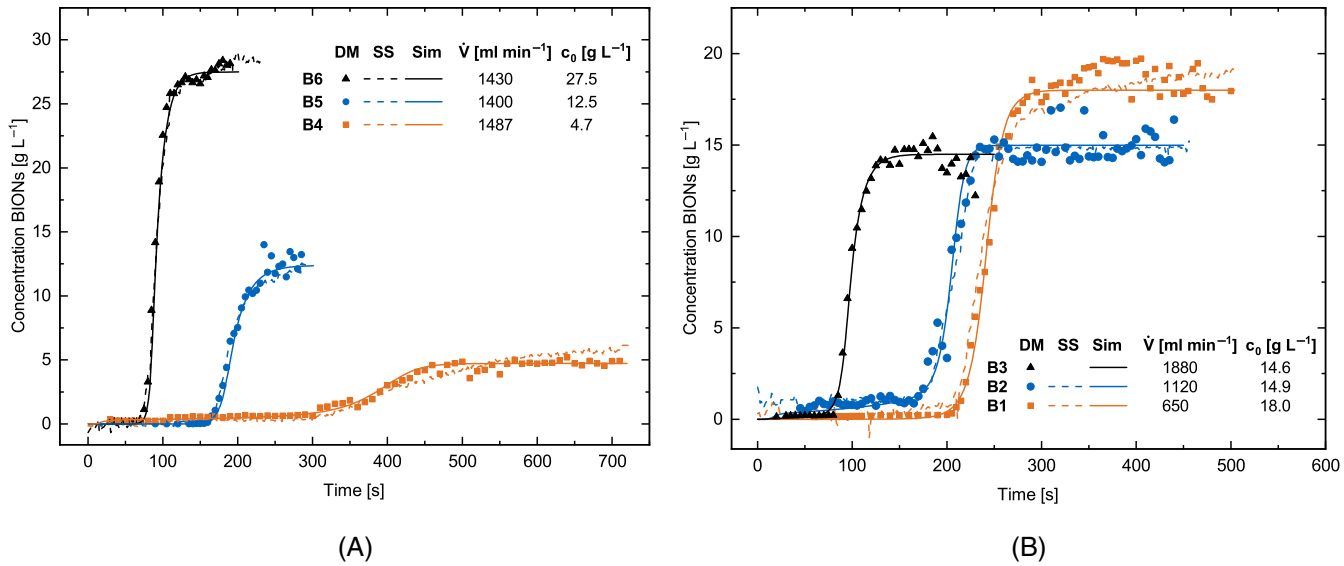

FIGURE 5 Experimental validation of model and soft-sensor performance through breakthrough experiments at varied (A) initial concentrations c_0 and (B) volume flows $\dot{V}$. Dry measurements (DM, dot line) were conducted for experimental validation, while the soft-sensor (SS, dashed line) was derived using data from the density sensor. BION batches 1 to 6 correspond to the curves B1 to B6. The simulation results (Sim) are depicted with solid lines.

concentration led to a quicker attainment of trapping saturation on the matrix.

The relationship between flow velocity and magnetic separation efficiency is effectively illustrated in Figure 5B, highlighting that increased velocity leads to premature matrix saturation and diminished magnetic separation efficiency. Additionally, the curves in Figure 5 underscore the impact of diverse BION size distributions. Specifically, Batch 4, characterized by a notably small particle-size distribution, exhibited early breakthrough in a portion of BIONs, as seen in Figure 5A (curve B4). Overall, a comparison between experimental results (points) and simulated data (solid curves) in Figure 5 demonstrates a high degree of agreement, affirming the reliability and accuracy of the model across a broad spectrum of input parameters. Moreover, the implementation of a soft-sensor (dashed curve) for real-time BION concentration calculation was validated. The experimental and simulation data closely align with the soft-sensor readings across all curves. However, it is noted that at the highest velocity in Figure 5A, the density sensor was unable to accurately measure the density, and therefore, this data point was excluded from the results.

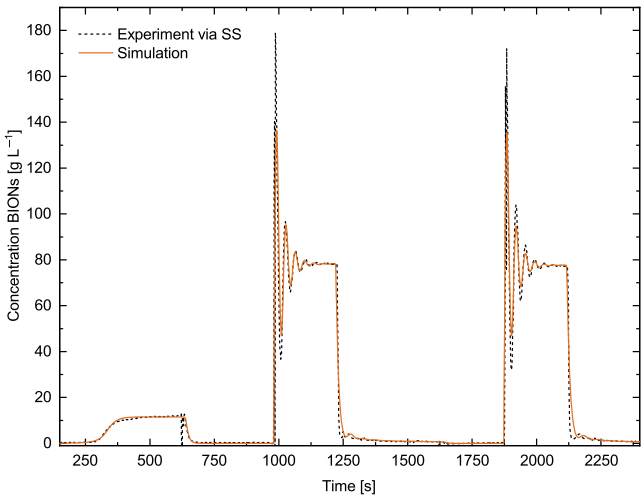

FIGURE 6 Model performance (solid orange line) validated against the experimental data obtained from soft-sensor (SS) measurements (dashed line), reflecting the sequence typically employed in protein purification protocols.

4.4.3 | Washing cycle

To further validate our model, we employed a washing protocol in the RS-HGMS as described in,[5] consisting of two washing cycles (Figure 6). After fully saturating the chamber with BIONs (0 to 620 s), each cycle involved: (1) flushing the chamber with pure water while retaining BIONs (620 to 970 s), (2) re-suspending BIONs by deactivating the magnet, rotating the rotor-stator discs, and recirculating the fluid (980 to 1225 s), and (3) recapturing BIONs while maintaining fluid circulation (1225 to 1650 s).

The experimental soft-sensor curve (dashed line) shows a BION breakthrough at around 265 s, allowing us to estimate the maximal BION capacity as 48.8 g. During the washing protocol (620 s), a sharp decrease in BION concentration occurred, coinciding with flushing the system while the magnet was active. Deactivation of the magnet, combined with rotor-stator disc rotation and continuous pumping, led to oscillations in BION concentration between 980 and 1225 s, due to system mixing dynamics, including the pipe and valves in the system. Reactivating the magnet at 1225 s, while maintaining loop pumping and stopping rotation, resulted in a rapid decrease in

concentration, stabilizing at approximately 0.46 g L^{-1}. This sequence was repeated in the next cycle.

A strong correlation is observed between our model's output (solid line) and the experimental data. However, minor discrepancies include (i) larger oscillation peaks in the experimental results and (ii) a slightly faster decline in BION concentration during the capture phase. These deviations may result from reduced back mixing in the actual system and possible inaccuracies in the density sensor under dynamic conditions, affecting the soft-sensor readings. Overall, the validation is satisfactory, confirming that our model accurately simulates RS-HGMS processes and magnetic particle behavior. The simulation time for the process in Figure 6 was 5.6 s.

5 | CONCLUSION

In our research, we developed a comprehensive multi-scale model capable of simulating the behavior of magnetic particles in HGMS processes for a diverse range of matrix geometries. This approach combines microscopic modeling of fluid flow and magnetic fields in complex HGMS configurations to derive functional relationships for magnetic particle trajectories and capture efficiency based on fluid dynamics and magnetic properties. These relationships were then integrated into macroscopic transport models, incorporating both convective and dispersive transport, allowing for rapid predictions of magnetic particle concentrations in full-scale HGMS processes. At the core of our work is a novel framework that can handle arbitrary matrix geometries, surpassing traditional wire-shaped matrices by generalizing a probability function to represent a wide range of matrix designs and configurations. This flexibility significantly broadens the applicability of our model to emerging HGMS applications, particularly in biotechnological processes, where new demands are placed on matrix design.

Our experimental validation demonstrated the high accuracy of the models in characterizing magnetic particle capture and transport in the RS-HGMS system. Magnetic particle concentrations were measured and compared with model outputs, confirming model accuracy through breakthrough curves and a washing protocol relevant to protein purification processes in biotechnology. However, it is crucial to note that our model incorporates a semi-empirical function for the deposition rate of magnetic particles onto the matrix. Additionally, the maximum filter capacity is a parameter requiring experimental calibration. Therefore, while our model is highly effective, it necessitates specific calibrations for different operational conditions to fully predict HGMS processes. A comprehensive prediction of the HGMS process would also require an in-depth analysis of the dynamic buildup of magnetic particles on the matrix and the derivation of a corresponding function for the macroscopic models.

Our model and methodology provide a valuable tool for optimizing HGMS processes and enabling in-silico optimization of chamber and matrix designs. With the ability to model diverse matrix geometries, this approach expands the scope for new applications requiring innovative matrix designs, such as bioprocessing. This enhances process optimization beyond traditional experiments, offering a faster, more cost-effective route to improve HGMS efficiency and effectiveness in practical applications.

AUTHOR CONTRIBUTIONS

Marko Tesanovic: conceptualization; methodology; software; data curation; investigation; validation; visualization; formal analysis; writing – original draft; writing – review and editing. **J. Pedro de Souza:** methodology; software; writing – review and editing. **Martin Z. Bazant:** methodology; writing – review and editing; supervision. **Sonja Berensmeier:** writing – review and editing; resources; project administration; supervision; funding acquisition.

ACKNOWLEDGMENTS

The authors gratefully acknowledge the support from the MIT-Germany Lockheed Martin Seed Fund and the MIT International Science and Technology Initiatives (MISTI). We also extend our appreciation to the TUM Global Incentive Fund for fostering international collaborations. Special thanks to Vivian Chen for her dedicated experimental work and valuable data collection, and to Stefan Hempfling and Paul Jacoby for their contributions to the simulation work. We also express our gratitude to Endress+Hauser Germany for their support in in-line analytics. Open Access funding enabled and organized by Projekt DEAL.

CONFLICT OF INTEREST STATEMENT

The authors declare the following financial interests/personal relationships which may be considered as potential competing interests: Marko Tesanovic reports travel was provided by Massachusetts Institute of Technology International Science and Technology Initiatives. J. Pedro de Souza reports travel was provided by the Massachusetts Institute of Technology International Science and Technology Initiatives. Martin Zdenek Bazant reports travel was provided by the Massachusetts Institute of Technology International Science and Technology Initiatives. Sonja Berensmeier reports travel was provided by the Massachusetts Institute of Technology International Science and Technology Initiatives. If there are other authors, they declare that they have no known competing financial interests or personal relationships that could have appeared to influence the work reported in this paper.

FUNDING INFORMATION

This work was supported by the German Federal Office for Agriculture and Food, Germany (BMLE 281A503A19).

DATA AVAILABILITY STATEMENT

All experimental data supporting the findings of this study are provided in the Supporting Information. The raw experimental data from Figures 5, 6, A1, A2, and A3 are tabulated in the Supporting Information. Most experimental data were measured in duplicates or triplicates to ensure reliability. For the breakthrough curves in Figure 5, individual measurements were conducted using two orthogonal methods: dry mass and a soft-sensor, enhancing data reliability and reproducibility. Our experimental data for the magnetic particle characteristics show good agreement with previous studies.[5]

ORCID

Marko Tesanovic https://orcid.org/0009-0006-6847-4968

REFERENCES

1. Franzreb M. *Magnettechnologie in der Verfahrenstechnik wässriger Medien*. tech. rep. Forschungszentrum Karlsruhe GmbH; 2003.
2. Kolm H. Research needs in magnetic separation. *IEEE Trans Magn*. 1976;12(5):450-454.
3. Hoffmann C. *Einsatz magnetischer Separationsverfahren zur biotechnologischen Produktaufarbeitung*. tech. rep. Forschungszentrum Karlsruhe GmbH; 2003.
4. Schwaminger SP, Schwarzenberger K, Gatzemeier J, Lei Z, Eckert K. Magnetically induced aggregation of iron oxide nanoparticles for carrier flotation strategies. *ACS Appl Mater Interfaces*. 2021;13(17):20830-20844.
5. Krolitzki E, Steck S, Nazifi A, Abt M, Schwaminger SP, Berensmeier S. How to design a low-cost pilot scale magnetic bioseparation process for protein separation from complex mixtures using in-line process analytics. *Sep Purif Technol*. 2023;323:124429.
6. Turco F, Wegelius A, Lind O, et al. Combined clarification and affinity capture using magnetic resin enables efficient separation of rAAV5 from cell lysate. *Mol Ther Methods Clin Dev*. 2023;30:394-402.
7. Ebeler M, Pilgram F, Wolz K, Grim G, Franzreb M. Magnetic separation on a new level: characterization and performance prediction of a cGMP compliant "rotor-stator" high-gradient magnetic separator. *Biotechnol J*. 2018;13(2):1700448.
8. Ebeler M, Lind O, Norrman N, Palmgren R, Franzreb M. One-step integrated clarification and purification of a monoclonal antibody using protein a mag Sepharose beads and a cGMP-compliant high-gradient magnetic separator. *New Biotechnol*. 2018;42:48-55.
9. Straton JA. *Electromagnetic Theory*. Wiley-VCH; 1941.
10. Watson J. Magnetic filtration. *J Appl Phys*. 1973;44(9):4209-4213.
11. Watson J. Approximate solutions of the magnetic separator equations. *IEEE Trans Magn*. 1978;14(4):240-245.
12. Gerber R, Watmough M. Magnetic separator equations. *IEEE Trans Magn*. 1982;18(6):1671-1673.
13. Li W, Zhou L, Han Y, Xu R. Numerical simulation and experimental verification for magnetic field analysis of thread magnetic matrix in high gradient magnetic separation. *Powder Technol*. 2019;355:300-308.
14. Tian Y, Cao Q. Effect of the number of magnetic matrices on particle capture in high gradient magnetic separation. *J Phys D Appl Phys*. 2023;57(4):045002.
15. Wang Y, Xue Z, Zheng X, Lu D, Sun Z. Matching relation between matrix aspect ratio and applied magnetic induction for maximum particle capture in transversal high gradient magnetic separation. *Miner Eng*. 2020;151:106316.
16. Zheng X, Sun Z, Wang Y, Lu D, Xue Z. Matching relation between matrix aspect ratio and applied induction for maximum particle capture in longitudinal high gradient magnetic separation. *Sep Purif Technol*. 2020;241:116687.
17. Lindner J, Menzel K, Nirschl H. Simulation of magnetic suspensions for HGMS using CFD, FEM and DEM modeling. *Comput Chem Eng*. 2013;54:111-121.
18. Choomphon-anomakhun N, Ebner AD, Natenapit M, Ritter JA. Simulation of dynamic magnetic particle capture and accumulation around a ferromagnetic wire. *J Magn Magn Mater*. 2017;428:493-505.
19. Herzig JP, Leclerc DM, Goff PL. Flow of suspensions through porous media—application to deep filtration. *Ind Eng Chem*. 1970;62(5):8-35.
20. Khashan SA, Furlani EP. Coupled particle–fluid transport and magnetic separation in microfluidic systems with passive magnetic functionality. *J Phys D Appl Phys*. 2013;46(12):125002.
21. Osborn JA. Demagnetizing factors of the general ellipsoid. *Phys Rev*. 1945;67(11):351-357.
22. Svoboda J. *Magnetic Techniques for the Treatment of Materials*. Springer; 1989:2.
23. Chen F. *Magnetically Enhanced Centrifugation for Continuous Biopharmaceutical Processing*. PhD thesis. Massachusetts Institute of Technology; 2009.
24. Neuringer JL, Rosensweig RE. Ferrohydrodynamics. *Phys Fluids*. 1964;7(12):1927-1937.
25. Khashan S, Furlani E. *Modeling Particle-Fluid Coupling and its Impact on Magnetic Particle Transport in Microfluidic Systems*. Tech Proc NSTI Nanotech; 2012.
26. Zapp Precision Metals GmbH. Ergste 1.4016IH Automotive Datasheet & Automation Technology. 2020.
27. Lucefine Group. Data-Sheet. *Steel*. 2015;1:4016.
28. Roth HC, Schwaminger SP, Peng F, Berensmeier S. Immobilization of Cellulase on magnetic Nanocarriers. *ChemOpen*. 2016;5(3):183-187.
29. Baerns M. *Technische Chemie*. Wiley-VCH; 2023.
30. Lim EWC, Feng R. Agglomeration of magnetic nanoparticles. *J Chem Phys*. 2012;136(12):124109.

SUPPORTING INFORMATION

Additional supporting information can be found online in the Supporting Information section at the end of this article.

How to cite this article: Tesanovic M, de Souza JP, Bazant MZ, Berensmeier S. Magnetic particle capture in high-gradient magnetic separation: A theoretical and experimental study. *AIChE J*. 2025;71(5):e18733. doi:10.1002/aic.18733

APPENDIX

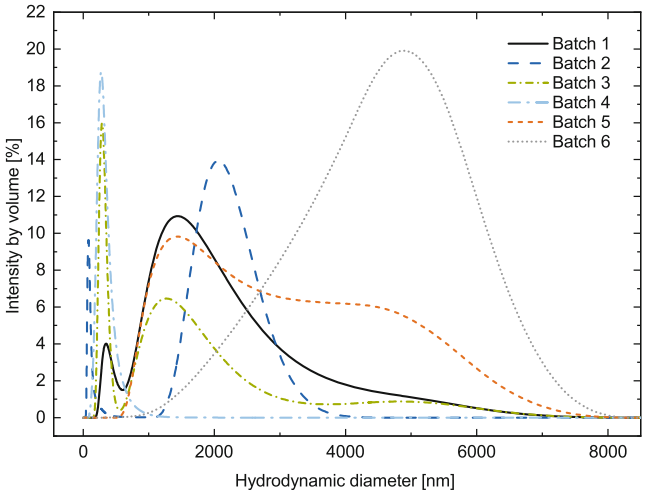

FIGURE A1 Particle-size distribution of BIONs (1 gL^{-1}) in pure water for six different batches with a conductivity smaller 200 $\mu S\ cm^{-1}$.

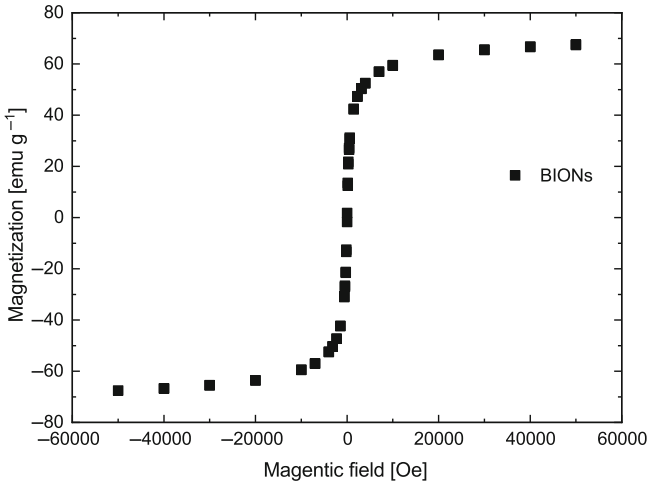

FIGURE A2 SQUID magnetization measurement conducted at 300 K between −40 and +40 kOe.

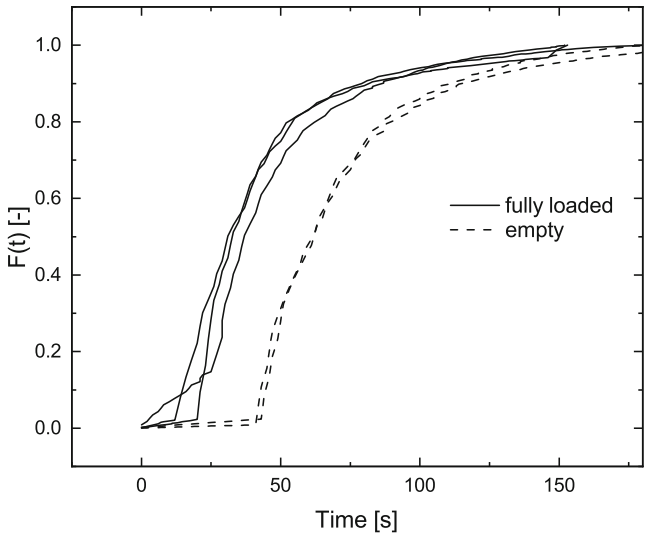

FIGURE A3 Residence time comparison in RS-HGMS chamber of a sodium chloride pulse in two distinct scenarios: An empty chamber (dashed curve) and a chamber fully loaded with BIONs (solid curve). The comparison highlights the impact of BIONs on the flow dynamics and the occupied volume by the slurry within the chamber.